



Cite this: DOI: 10.1039/c5nr06346a

Improving the photocatalytic hydrogen production of Ag/g-C₃N₄ nanocomposites by dye-sensitization under visible light irradiation†

Jiayi Qin,^a Jingpei Huo,^b Piyong Zhang,^b Jian Zeng,^a Tingting Wang^b and Heping Zeng^{*a,b}

Ag nanoparticles were deposited on the surface of g-C₃N₄ by a chemical reduction method to increase visible-light absorption via the localized surface plasmon resonance effect, resulting in the reduced recombination of photo-generated electron–holes and enhanced photocatalytic activity. The Ag/g-C₃N₄ composite with a Ag loading of 3 wt% has the optimum photoactivity that is almost 3.6 and 3.4 times higher than pure g-C₃N₄ and the same photocatalysis system which has been reported, respectively. Fluorescein was introduced as a photosensitizer and H₂ evolution soared to 2014.20 μmol g^{−1} h^{−1} and the rate is even about 4.8 times higher than that of the 3 wt% Ag/g-C₃N₄ composite. The chemical structure, composites, morphologies and optical properties of the obtained products are well-characterized by XRD, FTIR, TEM, EDS, XPS and UV-Vis DRS. Meanwhile, the photocatalyst exhibits high stability and reusability.

Received 15th September 2015,
Accepted 17th December 2015

DOI: 10.1039/c5nr06346a

www.rsc.org/nanoscale

Introduction

Photocatalytic toxic organic degradation or hydrogen generation using solar energy has been arousing intensive attention, which is a viable answer to environmental crises and energy consumption.^{1–7} Since the photolysis of water on the basis of TiO₂ was first discovered in 1972,^{8,9} as a new topic, semiconductor photocatalysis has increasingly been used for transforming solar energy into chemical energy.^{10,11} Subsequently, in this domain, photocatalysis based on semiconductors has arisen as one of the highest potential sciences and technologies.¹² So, many efforts have been made to discover green and renewable photocatalysts with a splendid visible

light response, making the utmost of the abundant solar power.

It is well known that graphitic carbon nitride (g-C₃N₄), as a metal-free and C-related photocatalyst, has been applied in hydrogen evolution and organics degradation gradually, because it is abundant and it has an appropriate band gap of *ca.* 2.7 eV.^{13–16} Besides, the electronic structure with π -conjugated graphitic planes formed by triazine units provides high activity, high stability and a visible light response.^{10,12,17–20} However, lack of absorption of the visible light beyond 460 nm and quick recombination of photo-induced carriers both have negative impacts on its photocatalytic effect. Coupling two semiconductors such as g-C₃N₄/TiO₂, g-C₃N₄/CdS, g-C₃N₄/MoO₃, g-C₃N₄/BiVO₄, g-C₃N₄/InVO₄ and g-C₃N₄/NiFe-LDH^{21–26} or preparing semiconductor-noble metal (such as Au, Ag, Pt) composites^{27–30} are commonly used to improve the catalytic efficiency and facilitate the separation of photo-generated electrons and holes.

Based on our previous research,^{3,7,11,32,55} a new composite was fabricated by embedding Ag nanoparticles into g-C₃N₄. Herein, a list of Ag loaded g-C₃N₄ heterostructures are prepared by thermal polycondensation of urea combined with the chemical reduction method. Owing to the localized surface plasmon resonance (LSPR) of silver nanoparticles, the as-prepared g-C₃N₄-based materials could improve the visible light photocatalytic activity significantly. Fundamentally, the strong local electromagnetic fields caused by the LSPR effect could accelerate the formation of h_{VB}^+ and e_{CB}^- .^{31,32} In addition,

^aGuangzhou Key Laboratory of Materials for Energy Conversion and Storage, School of Chemistry and Environment, South China Normal University, Guangzhou, 510006, P. R. China. E-mail: hpzeng@scut.edu.cn; Fax: +86-20-87112631; Tel: +86-20-87112631

^bState Key Laboratory of Luminescent Materials and Devices, Institute of Functional Molecules, School of Chemistry and Chemical Engineering, South China University of Technology, Guangzhou, 510641, P. R. China

†Electronic supplementary information (ESI) available: TEM images, TGA curves, PXRD and FTIR spectra, the recycling experiment of 3% Ag/g-C₃N₄, the specific process for H₂ production, the diagram for the rate of hydrogen generation vs. the amount of fluorescein, the figure for the photocatalytic hydrogen production testing system, tables of contrast experiments for photocatalytic hydrogen generation and elemental composition of the CN in all the samples. See DOI: 10.1039/c5nr06346a

Fermi levels of the metal nanoparticles not only contribute to the formation of a Schottky barrier to support separation of photo-induced electron-hole pairs, but also make the transferred electrons shift to a more negative potential, thereby elevating the quantum efficiency of g-C₃N₄ and keeping the reducibility of e_{CB}⁻ that migrates from g-C₃N₄.^{33–36}

Recently, Ge *et al.*³³ prepared Ag-g-C₃N₄ composites by calcining melamine and a mixture of g-C₃N₄ with AgNO₃, and its maximum hydrogen production rate is 101.05 μmol g⁻¹ h⁻¹. Bai *et al.*²⁸ developed a novel core-shell Ag@C₃N₄ nanostructure by heating dicyandiamide followed by photoreduction to form Ag nanoparticles, then core-shell Ag@C₃N₄ samples were prepared *via* a reflux treatment of Ag nanoparticles with g-C₃N₄ for 3 h. Finally, the visible-light-induced highest H₂ generation rate is 25.2 μmol g⁻¹ h⁻¹. Compared with the above-mentioned methods and pure g-C₃N₄, Ag/g-C₃N₄ nanocomposites reported in this work show a more prominent photocatalytic ability for H₂ evolution in the presence of a sacrificial agent under visible light irradiation, in which the rate of H₂ production can reach 344.51 μmol g⁻¹ h⁻¹. Besides, the synthetic method to obtain a novel porous Ag/g-C₃N₄ structure is much more facile, cheaper and consumes less energy.

As we all know, organic dyes have been applied in dye sensitized solar cells (DSSCs) for taking advantage of solar energy more effectively. Over the past few years, dyes have been gradually used in the photocatalytic hydrogen production as a visible light harvesting molecule to extend the possibility of the reaction.³⁷ Recently, Zhang *et al.*³⁸ reported an Eosin Y-sensitized attapulgite nanocrystal that reduces water for hydrogen production effectively and the highest H₂ generation rate is *ca.* 800 μmol g⁻¹ h⁻¹. However, the hydrogen generation rate reaches 1370 μmol g⁻¹ h⁻¹ after Ag loading, ascribed to the Ag-loading promotion. Besides, Yuan *et al.*³⁹ provided Zr-containing MOFs of UiO-66 octahedra sensitized by Erythrosin B dye and it has 0.25% quantum efficiency at 420 nm with 460 μmol g⁻¹ h⁻¹ hydrogen production efficiency. Moreover, Jia *et al.*⁴⁰ tried to use Eosin Y as a sensitizer for single layer MoS₂, which displayed excellent activity and stability with H₂ evolution 7.3 times higher than that of pure MoS₂. Meanwhile, zinc phthalocyanine derivative sensitized g-C₃N₄ with loaded Pt was found for hydrogen production and asymmetric zinc phthalocyanines have better photosensitization on g-C₃N₄ than symmetric structures.⁴¹

Fluorescein, a xanthene dye, has appropriate excitation and emission wavelengths in the visible region, and a high fluorescence quantum yield in aqueous solution.⁴² It has been used widely for labeling biomolecules and tracking oceanography.⁴³ According to the literature,⁴⁴ the electron transfer rate from the LUMO of fluorescein to g-C₃N₄ is comparatively higher than from other dyes. So, fluorescein was selected to work as a photosensitizer to improve the activity of the photocatalyst. Under visible light irradiation, the electrons transfer from the HOMO to the LUMO of the fluorescein molecule, generating electron-hole pairs. The ground energy level is located in the band gap of g-C₃N₄ and the electronic excited

state is resonant with the CB of g-C₃N₄. Also, the more negative LUMO potential than that of CB on g-C₃N₄ ensures quick electronic transfer.⁴³ During the catalytic process, fluorescein exhibits fairish photostability and thermal stability.⁴⁵ Eventually, H₂ production soars to 2014.20 μmol g⁻¹ h⁻¹ that could be called a higher level in reported values.

The chemical structures and optical properties, as well as morphologies were characterized by transmission electron microscopy (TEM), scanning electron microscopy (SEM), energy dispersive spectrometry (EDS), Brunauer–Emmett–Teller (BET) analysis, X-ray diffraction (XRD), Raman spectra, UV-vis and photoluminescence (PL) spectroscopy. The element species and their chemical status were investigated by X-ray photoelectron spectroscopy (XPS). Furthermore, the possible mechanism for the photocatalysis process under sunlight was also put forward.

Results and discussion

Crystal structure and composition

The XRD patterns of g-C₃N₄ and Ag/g-C₃N₄ photocatalysts with different silver mass contents are shown in Fig. 1. As can be seen in pure g-C₃N₄, the peaks at 13.1° for the (100)² diffraction plane and at 27.4° for the (002)² diffraction plane are derived from the in-plane structural packing of tri-s-triazine units and interplanar stacking peaks of conjugated aromatic systems, respectively.^{21,46,47} According to JCPDS 87-1526, g-C₃N₄ possesses XRD peaks at 13.1° for (100) and 27.8° for (002).⁴⁸ In the present case, the 27.4° peak is slightly shifted towards a lower angle, which indicates that the interplanar distance between the conjugated aromatic systems increases.¹⁶ In the 1SCN (1% Ag/g-C₃N₄), there are no obvious diffraction peaks of Ag due to its relatively low levels. As the deposition of silver increases from 3% to 9%, the intensity of the characteristic peaks indexed to Ag (JCPDS no. 089-3722)²⁸ appears stron-

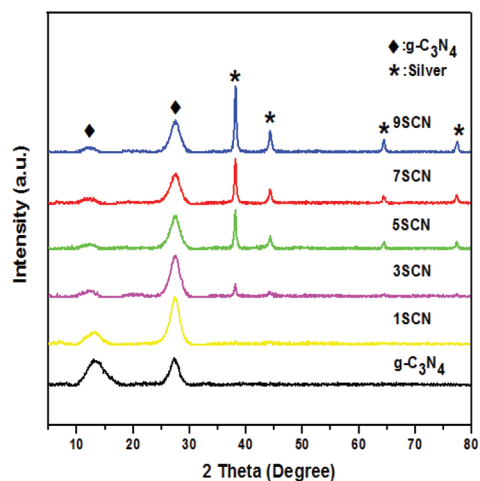


Fig. 1 XRD patterns of the as-prepared pure g-C₃N₄ and Ag/g-C₃N₄ composites with different doping amounts of Ag.

ger gradually, while the diffraction peak at 13.1° becomes weaker than bare $g\text{-C}_3\text{N}_4$, which indicates that bulk $g\text{-C}_3\text{N}_4$ nanosheets are exfoliated during the introduction of Ag and the crystal structures of the samples are also affected by the plasmonic behavior of Ag.²⁸ Furthermore, no other diffraction peaks from impurities can be observed, proving that $\text{Ag}/g\text{-C}_3\text{N}_4$ composites remain pure. Also may be some existing minor amount of Ag_2O attributed to metallic Ag oxidation could not be detected in the strongest XRD signal.

Fig. 2 depicts the FTIR spectrograms of the pure $g\text{-C}_3\text{N}_4$ and the $\text{Ag}/g\text{-C}_3\text{N}_4$ composites with a mass ratio of 3%. For the bare $g\text{-C}_3\text{N}_4$ sample, the feature peak positions are broadly in line with the results presented in the previous reports. The peak at 1638 cm^{-1} could be ascribed to C–N stretching and the four peaks at 1241 cm^{-1} , 1326 cm^{-1} , 1411 cm^{-1} and 1570 cm^{-1} can be attributed to the aromatic C–N stretching vibration.^{47,49} The absorption peak at 807 cm^{-1} accords with the characteristic breathing mode of triazine units.^{50,51} The broad peak in the range of $3000\text{--}3500\text{ cm}^{-1}$ corresponds to the N–H stretching vibration of uncondensed amino groups and O–H vibration from adsorbed water on the surface.^{52,53} All main characteristic vibration IR peaks related to $g\text{-C}_3\text{N}_4$ can be distinctly found in 3SCN, suggesting that the overall structure of $g\text{-C}_3\text{N}_4$ remains intact after doping Ag nanoparticles.

The XPS spectra of the as-synthesized 3SCN nanocomposite sample were analyzed to further confirm the chemical composition and the status of the elements (Fig. 3). The survey spectrum of the $\text{Ag}/g\text{-C}_3\text{N}_4$ nano-composite sample is shown in Fig. 3a, which indicates that the composite is composed primarily of C, Ag, N and a small amount of O elements. A relatively small amount of oxygen remains in the as-prepared sample; this may be caused by the partial oxidation of Ag into Ag_2O and surface absorption.³³ Fig. 3b displays the high-resolution XPS spectra of C 1s, the peak located at 284.6 eV attributed to sp^2 C atoms in N-C=N and C–C bonding of the surface exotic carbon from the detecting instrument, the other one centered at 288.0 eV can be assigned to the sp^3 hybridized carbon bonded to N in the C-(N)_3 of $g\text{-C}_3\text{N}_4$.^{13,33,36,46} The XPS spectrum of N 1s (Fig. 3c) was separated into three peaks at binding energies of 398.5 , 401.0 , 404.5 eV , which can be

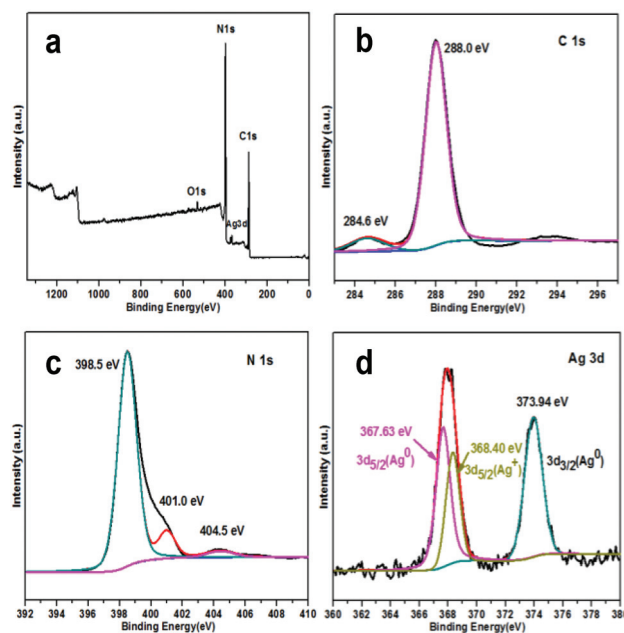


Fig. 3 XPS spectra of the as-prepared 3SCN composite.

ascribed to C-N=C , N-(C)_3 and N-H , respectively, referring to previously reported results.^{36,46} The doublet of Ag 3d also can be deconvoluted into three typical peaks (Fig. 3d), in which the peaks at 367.63 eV and 373.94 eV belong to $\text{Ag } 3d_{5/2}(\text{Ag}^0)$ and $\text{Ag } 3d_{3/2}(\text{Ag}^0)$, respectively. However, the remaining one at 368.40 eV is the characteristic peak of $\text{Ag } 3d_{5/2}(\text{Ag}^+)$ produced on oxidation of a little metallic Ag.^{13,36} From the integration areas in Fig. 3d, the ratio of $\text{Ag}^0:\text{Ag}^+$ is *ca.* 3.5, so the amount of Ag^+ is minuscule in the case that summation of both is very low. The ICP-MS technology was utilized to confirm the total weight percentage of the silver element in the composite, and the silver content is 369.14 ppb . So, the quality of silver is 0.1433 g , which is about 2.95% of the weight of $g\text{-C}_3\text{N}_4$ in 3SCN. The result is in close proximity to the theoretical value of 3% .

Morphology

Fig. 4 shows the SEM images of pure $g\text{-C}_3\text{N}_4$ and $\text{Ag}/g\text{-C}_3\text{N}_4$ composites with different amounts of Ag loading as well as EDS of the prepared 5SCN sample. $g\text{-C}_3\text{N}_4$ (Fig. 4a) exhibits planar and poriferous structures. After introducing Ag nanoparticles, the $\text{Ag}/g\text{-C}_3\text{N}_4$ composites show a tremella-like structure and the thickness of the layers become thinner as the silver content increases from 1% to 5% (Fig. 4b–d), which suggests that the original nanoplates of $g\text{-C}_3\text{N}_4$ were skived and Ag was dispersed on the surface of $g\text{-C}_3\text{N}_4$ to form a closely conjugated structure, in accordance with the XRD results. Nevertheless, when Ag loading amounts reach 7% or 9% (Fig. 4e and f), the aggregation of Ag nanoparticles will happen on the sample surface, as a result, the obtained agglomeration structures may lead to a lower

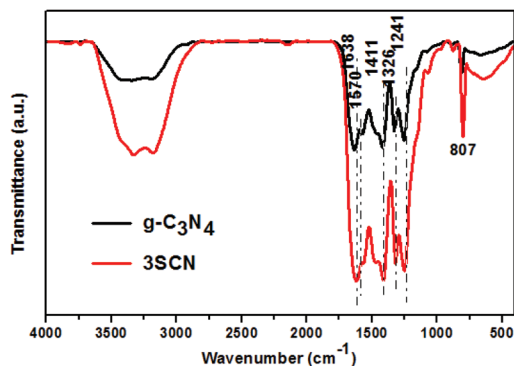


Fig. 2 FTIR spectra of the as-prepared pure $g\text{-C}_3\text{N}_4$ and 3SCN.

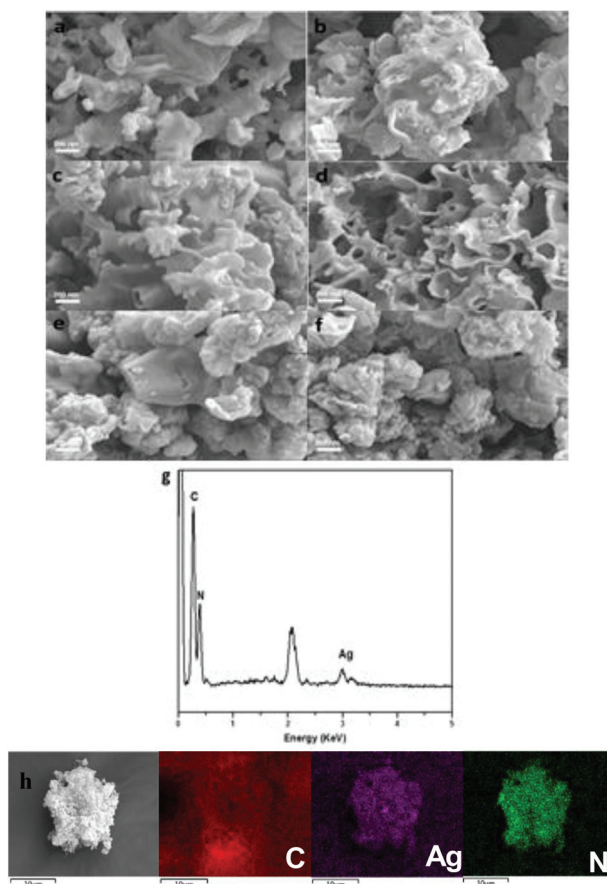


Fig. 4 SEM images of the as-prepared Ag/g-C₃N₄ composites: (a) pure g-C₃N₄, (b) 1SCN, (c) 3SCN, (d) 5SCN, (e) 7SCN, (f) 9SCN; (g) EDS spectra of the 5SCN sample; (h) elemental mapping pattern of 5SCN.

quantum efficiency.⁹ EDS and elemental mapping of 5SCN reveal that the sample mainly contains three elements (C, N and Ag) after removing extra elements introduced from the environment.

The morphology and microstructures of Ag/g-C₃N₄ photocatalysts were further investigated by TEM. Fig. 5a and b show that the 3SCN composite has a layered and porous structure with clear Ag nanoparticles well sited on it. From Fig. 5c, we can see that g-C₃N₄ demonstrates its characteristic platelet-like morphology and jagged edges.¹² The HRTEM images (Fig. 5d and e) reveal that Ag particles are well distributed on g-C₃N₄ and a very close connection existed between Ag and g-C₃N₄ to form a heterostructure, guaranteeing the charge transfer in the space smoothly. Moreover, the lattice spacing of Ag was measured as $d = 0.24$ nm, conforming to the (111) crystallographic plane of zero-valent Ag (JCPDS no. 089-3722).²⁸ There are no lattices of Ag₂O observed in the limited field due to its very low levels. Fig. 5f illustrates the size distribution of Ag nanoparticles in 3SCN by calculating the diameters of 308 dark spots from TEM images (Fig. S1†). As we can see, the diameters of Ag nanoparticles are mainly 2–5 nm, and the mean diameter is about 3.45 nm.

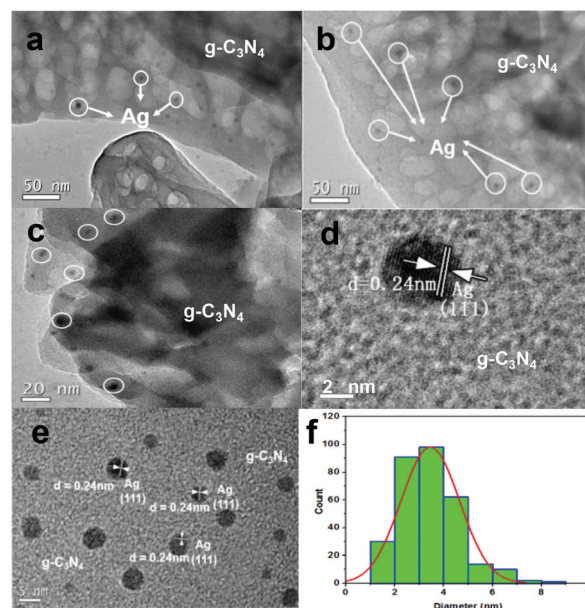


Fig. 5 TEM images of the as-prepared Ag/g-C₃N₄: (a, b) 3SCN, (c) magnification of 3SCN, (d, e) high-resolution TEM image of 3SCN, (f) size distribution histogram of Ag nanoparticles of 3SCN.

BET specific surface area and pore textural analysis

From Table 1, it can be observed that the samples have differences in physical properties. Compared with g-C₃N₄, doping Ag samples have smaller S_{BET} . This is because the introduced Ag nanoparticles may occupy some space of nanosheets and fill some pores of g-C₃N₄. Among all the Ag/g-C₃N₄ composites, 3SCN exhibits the largest surface area, pore volume and size that is even bigger than pure g-C₃N₄. 3SCN has more active sites on the surface to absorb more molecules; this may be because appropriate amounts of silver particles were embedded in the interlayer of g-C₃N₄, leading to the nanolayer becoming thinner and the number of pores relatively increased. As the loading amount of silver continues to rise, Ag particles induced the aggregation of g-C₃N₄ nanosheets and filled more pores, which results in reduced S_{BET} , pore volume and average pore size. But 1SCN also has a smaller pore volume and an average pore size, this may result from the added bits of silver which are mainly distributed in the pores.

Table 1 S_{BET} , pore volume and average pore size of the as-prepared samples

Sample	S_{BET} (m ² g ⁻¹)	Pore volume (cm ³ g ⁻¹)	Average pore size (nm)
g-C ₃ N ₄	29.6	0.027	3.6
1SCN	23.8	0.013	2.2
3SCN	25.4	0.035	5.4
5SCN	18.1	0.018	4.1
7SCN	18.0	0.017	3.8
9SCN	13.7	0.007	2.1

Optical properties

To investigate the optical properties of pure $g\text{-C}_3\text{N}_4$ and the as-prepared $\text{Ag}/g\text{-C}_3\text{N}_4$ composites, UV-vis DRS, PL and Raman spectra were recorded at room temperature. As shown in Fig. 6a, the characteristic absorption edge of pristine $g\text{-C}_3\text{N}_4$ is at approximately 460 nm, originating from its intrinsic band gap of 2.7 eV,¹⁰ which has limited visible light absorption ability for itself. After the introduction of Ag nanoparticles on the surface of $g\text{-C}_3\text{N}_4$, the composites show a broad absorption peak from 410 to 520 nm due to the surface plasmon resonance of Ag NPs, in turn, the enhanced absorption gives strong evidence that Ag NPs exist in the samples.^{9,54} The intensity of absorption increases gradually with the increasing Ag amount from 1, 3, 5 to 7 wt%, suggesting that a greater number of Ag can modify the surface to enhance the surface electron charge and light capture. However, the absorption of 9SCN is lower than that of 5SCN and 7SCN, this may be caused by the aggregation of silver nanoparticles on the sample surface.

To reveal the electron-hole separation properties, PL emission spectra were used to study the behavior of electron-hole pairs. Fig. 6b shows PL spectra of all $\text{Ag}/g\text{-C}_3\text{N}_4$ samples with that of $g\text{-C}_3\text{N}_4$ for comparison. The excitation wavelength of the PL spectra is set at 330 nm and the main emission peak of all samples is centered at around 440 nm. In the spectra, the emission intensity of pure $g\text{-C}_3\text{N}_4$ is highest, while that for $\text{Ag}/$

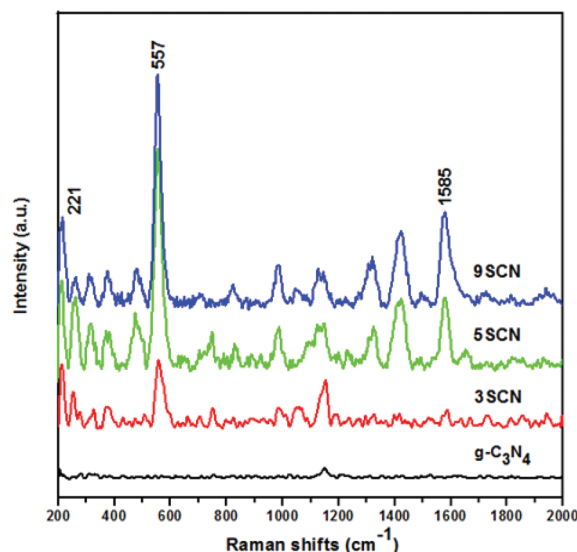


Fig. 7 Raman spectra of pure $g\text{-C}_3\text{N}_4$, 3SCN, 5SCN and 9SCN.

$g\text{-C}_3\text{N}_4$ composites was comparatively lower, which indicates that the recombination of electrons-holes is restrained effectively. This is because photo-generated electrons could transfer to Ag *via* the interface to accelerate the charge separation.⁵⁵ However, 3% is the optimal deposition amount to suppress recombination. As the silver loading increases to a certain degree, Ag NPs aggregate on the surface and conversely work as recombination centers to reduce suppression.⁹ This is why 5SCN, 7SCN and 9SCN have a lower photocatalytic activity for hydrogen generation.

Fig. 7 shows the Raman spectra of pure $g\text{-C}_3\text{N}_4$, 3SCN, 5SCN and 9SCN samples. There is no significant Raman signal observed on pure $g\text{-C}_3\text{N}_4$, but a clear Raman spectrum was first detected on 3SCN. The characteristic peaks at 1585 and 557 cm^{-1} are derived from the enhanced Raman spectrum of $g\text{-C}_3\text{N}_4$. The band at 1585 cm^{-1} corresponds to the $\text{C}=\text{N}$ stretching vibration of $g\text{-C}_3\text{N}_4$, which is also defined as a graphitic G band, indicating the formation of a graphite-like structure, while the one at 557 cm^{-1} belongs to the in-plane symmetrical stretching vibration of heptazine heterocycles.⁵⁶ In comparison with that of $g\text{-C}_3\text{N}_4$, the stepwisely enhanced two peaks indicate that the vibration intensity of the graphitic structure is stronger, which is attributed to the SERS effect of Ag NPs with appropriate shapes and sizes. Furthermore, the peak at 221 cm^{-1} in $\text{Ag}/g\text{-C}_3\text{N}_4$ composites symbolizes Ag-N symmetric vibration mode.⁵⁷ The results convincingly demonstrate that an interaction exists between Ag and $g\text{-C}_3\text{N}_4$ molecules to facilitate charge transfer.

Photocatalytic H_2 production and stability

The photocatalytic hydrogen evolution ability of the samples was evaluated under visible light similar to solar light irradiation, which is shown in Fig. 8a. Compared with pure $g\text{-C}_3\text{N}_4$, the $\text{Ag}/g\text{-C}_3\text{N}_4$ composites with different mass ratios

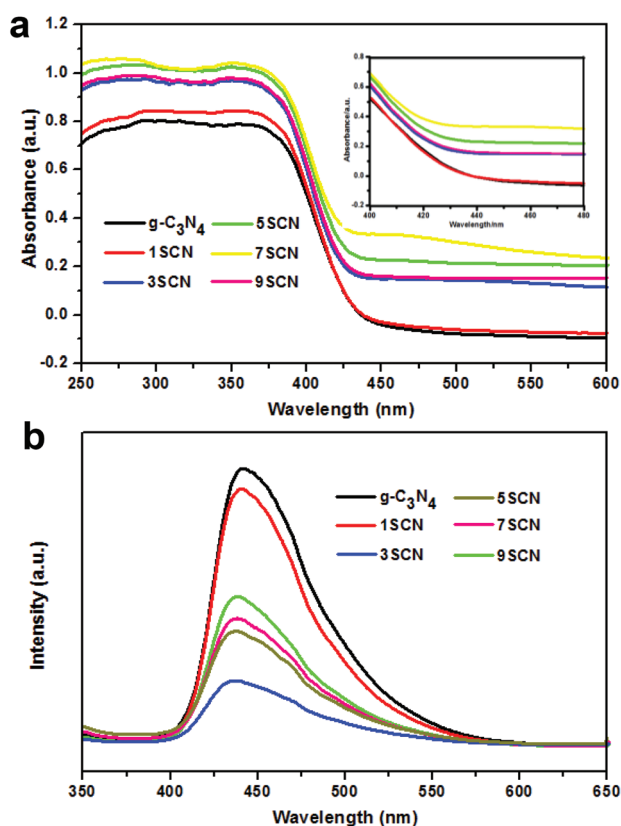


Fig. 6 (a) UV-vis DRS and (b) PL spectra of pure $g\text{-C}_3\text{N}_4$ and $\text{Ag}/g\text{-C}_3\text{N}_4$ composites.

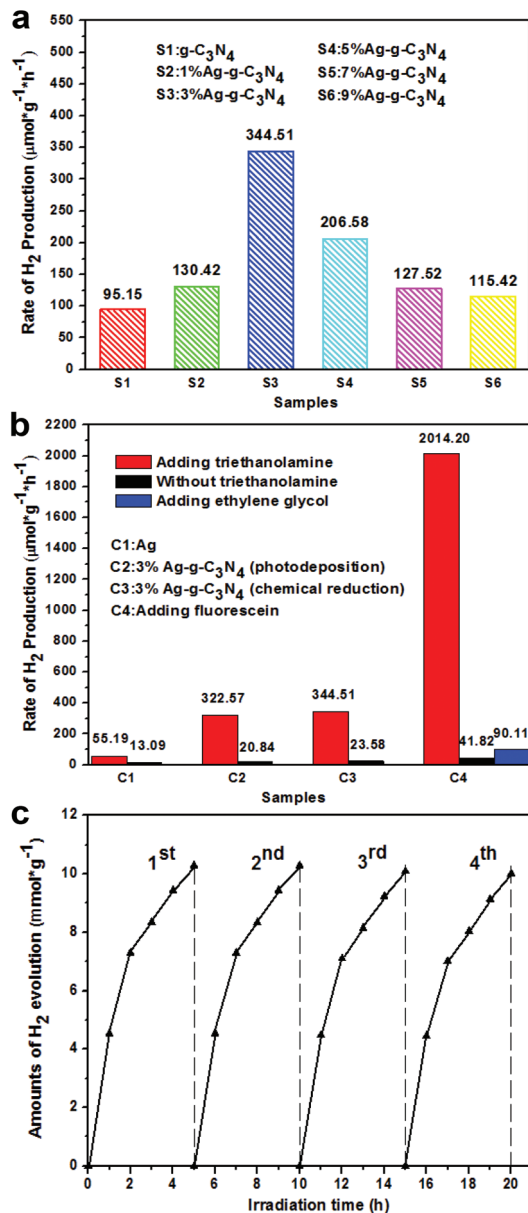


Fig. 8 Photocatalytic activity of the photocatalysts (0.005 g) for contrast under visible light similar to solar light irradiation: (a) H₂ evolution rates of g-C₃N₄ and Ag/g-C₃N₄ composites with different mass ratios in an aqueous solution (70 mL) containing TEOA (10 mL) as the sacrificial agent (irradiation time = 3 h); (b) H₂ evolution rates of Ag nanoparticles, 3SCN by photodeposition, 3SCN by chemical reduction and 3SCN by chemical reduction with fluorescein (0.005 g) in a 70 mL aqueous solution with and without 10 mL sacrificial agent (irradiation time = 3 h); (c) recycling test of the obtained 3SCN by chemical reduction with fluorescein (0.005 g) and 10 vol% TEOA for photo-catalytic hydrogen production (irradiation time = 20 h).

show higher photocatalytic activities and the highest photocatalytic H₂ production efficiency was realized with 3SCN (344.51 μmol g⁻¹ h⁻¹). This is 3.62 times higher than that of g-C₃N₄ (95.15 μmol g⁻¹ h⁻¹). However further increasing the content of Ag nanoparticles over 3 wt% results in a significant decrease in the photocatalyst activity, such as with 5SCN,

7SCN and 9SCN. This may be because they have a higher absorption of light than 3SCN, although (Fig. 6a) excessive silver particles adversely become recombination centers for photo-induced charges as mentioned above (Fig. 6b).

For practical applications, the 3SCN composite was selected as the representative sample to investigate the stability of Ag/g-C₃N₄ materials (Fig. S3†). The hydrogen generation efficiency in the third hour of every course was largely improved, exhibiting excellent catalytic performance of 3SCN after two hours of irradiation. No obvious deactivation of the catalytic activity was observed for 3SCN upon circulation duration, suggesting that the as-prepared Ag/g-C₃N₄ heterostructures had considerable stability and repeatability for hydrogen evolution under sunlight irradiation.

In order to explore how Ag, the sacrificial agent, choice of the loading method and fluorescein influence the hydrogen generation, a series of control experiments were performed under identical illumination conditions with results shown in Fig. 8b. As we can see, firstly, just only a little hydrogen evolution from water splitting was observed without a sacrificial agent in all experiments. This proves that a sacrificial agent is important in the photocatalytic hydrogen production process. TEOA as a sacrificial agent could consume photo-generated holes of g-C₃N₄ to hinder charge recombination, and thus more photo-generated electrons were used in the photocatalytic hydrogen evolution to enhance photoactivity. Secondly, Ag nanoparticles could be obtained from Group 1 (Table S2†) after an hour of illumination,² which was a new discovery, Ag nanoparticles can catalyze hydrogen generation by itself, but the catalytic capacity of individual Ag or g-C₃N₄ (Fig. 8a) is very low. When a synergistic effect existed between Ag and g-C₃N₄, Ag nanoparticles work as a sink for photogenerated electrons transferred from g-C₃N₄ and reinforce their energy by surface plasmon resonance to improve hydrogen production. Thirdly, two alternative means will be provided in the deposition of Ag, one is chemical reduction, and another is photodeposition (Group 2, Table S2†). 3SCN obtained by chemical reduction above achieves a little bit larger value (344.51 μmol g⁻¹ h⁻¹) than by photodeposition (322.57 μmol g⁻¹ h⁻¹). This may be interpreted as the chemical reduction method making the heterostructure between Ag and g-C₃N₄ combine more firmly. Finally, the H₂ production rate sharply augments to 2014.20 μmol g⁻¹ h⁻¹ after 0.005 g of fluorescein was added as a photosensitizer (Group 3, Table S2†), implying that fluorescein molecules were adsorbed on the surface of g-C₃N₄ to govern the broad visible light harvesting and conversion.⁵⁹ Fig. S4† shows the effect of the amount of fluorescein on the photocatalytic hydrogen evolution of 3SCN, and the photoactivity reaches a maximum when fluorescein is 0.005 g with a fluorescein concentration of about 2.1×10^{-4} mol L⁻¹. When EG as a sacrificial agent is used in Group 3, the H₂ production rate is only 90.11 μmol g⁻¹ h⁻¹. This is because TEOA is the optimized sacrificial agent for g-C₃N₄ for H₂ production.^{19,46,60} In the recycling test of 3SCN obtained by chemical reduction with fluorescein (Fig. 8c), as can be seen, the amount of hydrogen evolution per hour gradually

decreased during each cycle, due to the oxidation of fluorescein and consumption of TEOA as electron donors. However, in the four cycles, the catalytic effect of each period remained fairly consistent, indicating that the photocatalyst with fluorescein is reusable. Furthermore, after the first cycle reaction, the photocatalyst was recovered by centrifugation and subjected to powder XRD and FTIR measurements, respectively.⁶¹ There is a slight difference in both the PXRD and FTIR spectra (Fig. S5†).

Possible photocatalytic mechanism

Based on the above analysis, the electron transfer mechanism of the Ag/g-C₃N₄ heterostructure is given in Fig. 9 to help understand the photocatalytic process. According to previous reports, g-C₃N₄ is an n-type semiconductor with the redox potential of the conduction band (CB) and the valence band located at -1.3 eV and $+1.4$ eV vs. NHE,¹³ respectively. It can be seen that the LUMO of fluorescein is more negative than the CB of g-C₃N₄, meanwhile the HOMO of fluorescein is more positive than the redox potential of TEOA.⁵⁹ Upon visible light irradiation, both fluorescein and g-C₃N₄ could be excited, and then electrons from fluorescein were injected into the CB of g-C₃N₄ easily with the help of SPR. Then the electrons quickly migrate to Ag nanoparticles with the Fermi level at $+0.4$ eV vs. NHE,³⁶ which matches with the energy level of g-C₃N₄. The electrons accumulate on Ag nanoparticles to create a Schottky barrier that best inhibits the recombination of photo-generated electrons and holes. The strong local electromagnetic field induced by the SPR effect of Ag nanoparticles can enhance the captured electron energy and transfer rate, making them react with H⁺ for H₂ production more easily. Simultaneously, the photo-induced holes of fluorescein and g-C₃N₄ can be packed by electrons from TEOA for reuse. On

the other hand, the SPR effect strengthens the sunlight harvesting capacity of the photocatalysts, hence the generation rate of photo-excited carriers is speeded up. However, as mentioned above (Fig. 6), the superfluous Ag nanoparticles deposited on g-C₃N₄ have no obvious effect on further improving the catalytic activity, this is caused by the aggregation or production of new recombination centers. It is worth noting that electrons affected by surface plasma resonance include photo-generated electrons transferred from g-C₃N₄ and the excited electrons on Ag nanoparticles initially. As discussed above, Ag nanoparticles have a weak catalytic hydrogen production ability, as a result that e_{SPR}^- provided to H⁺ is insufficient in the absence of electrons from g-C₃N₄. The specific process of H₂ production is summarized in Fig. S6.†

To further verify the above photocatalytic conjecture, the transient photocurrent responses are recorded for g-C₃N₄, Ag/g-C₃N₄ and 3SCN-fluorescein composite photoelectrodes. Fig. 10a shows $I-t$ curves for the as-prepared film electrodes with three on-off intermittent visible-light irradiation cycles. It is clear that photocurrent responses appear in all of the electrodes instantly as soon as light is turned on, but are then quickly decreased to near zero once the light is off, which is stable and reproducible. Under the same irradiation conditions, the photo-current value of the 3SCN electrode is about 1.8 times as high as that of pristine g-C₃N₄, indicating that there is less recombination and faster photogenerated electron migration on 3SCN, ascribed to surface interactions between Ag and g-C₃N₄.⁴⁶ Additionally, the dye-sensitized Ag/g-C₃N₄ electrode shows a much higher photocurrent value which is about twice that of 3SN, suggesting that the photo-generated electrons from fluorescein are also involved in the electron transfer process and transferred to the CB of g-C₃N₄ efficiently.

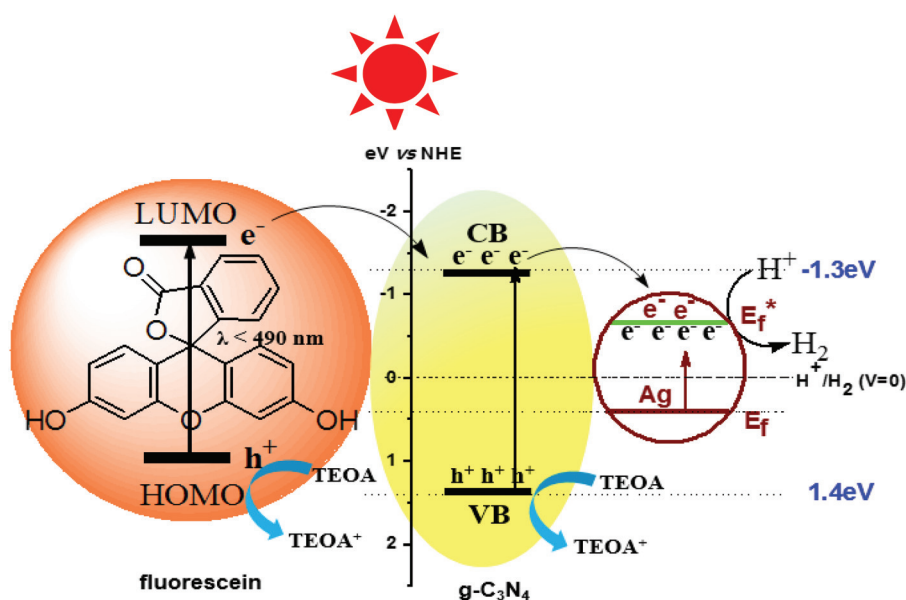


Fig. 9 Schematic illustration for charge separation and transfer over the Ag/g-C₃N₄ composite with fluorescein.

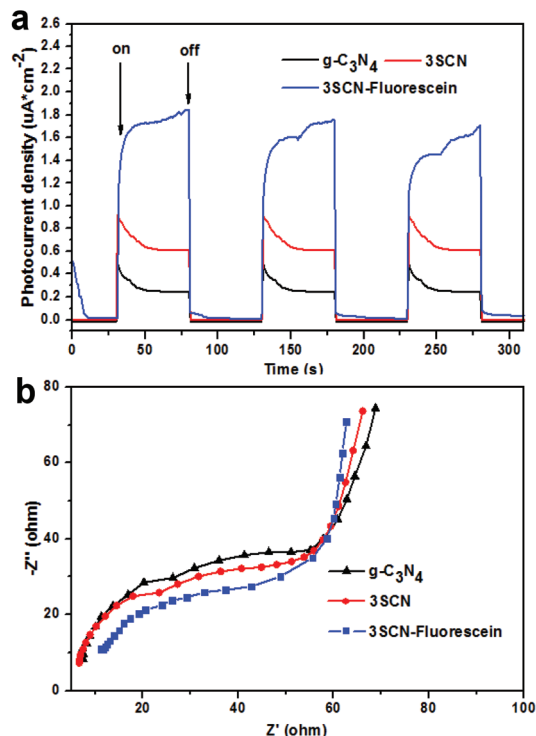


Fig. 10 (a) The transient photocurrent of pure $\text{g-C}_3\text{N}_4$, 3SCN and 3SCN-fluorescein under 300 W Xe-lamp irradiation without cutoff filters at 0.0 V bias vs. Ag/AgCl and (b) EIS of pure $\text{g-C}_3\text{N}_4$, 3SCN and 3SCN-fluorescein.

EIS is an available method to study the charge transfer efficiency and interface reaction ability.^{34,58} Fig. 10b reveals the Nyquist plots of $\text{g-C}_3\text{N}_4$, 3SCN and 3SCN-fluorescein, which correspond to their charge transfer resistance. The smaller diameter implies the lower impedance and faster interface charge transfer. The 3SCN-fluorescein has the smallest diameter and 3SCN shows a smaller diameter than $\text{g-C}_3\text{N}_4$ in the middle frequency region. The result accords with that obtained by the photocurrent.

In order to confirm that fluorescein molecules on Ag/ $\text{g-C}_3\text{N}_4$ composites dominate the enhancement of the photoactivity, XRD, UV-vis DRS and PL spectra were recorded. Fluorescein was mixed by the grinding method. As shown in Fig. 11a, compared with 3SCN, the spectrum of 3SCN-fluorescein exhibited additional characteristic peaks corresponding to fluorescein, confirming the presence of fluorescein on the 3SCN composite. The UV-vis diffuse reflectance absorption spectra (DRS) of 3SCN and its sensitized products are shown in Fig. 11b. Apparently, 3SCN-fluorescein shows obvious red/NIR light (550–750 nm) absorption ability, which efficiently extends the light-harvesting ability of 3SCN. Moreover, PL spectra (Fig. 11c) were measured to show the electron transfer between every component. The emission intensity of pure fluorescein is strong due to fast carrier recombination, and a distinct quenching can be observed on $\text{g-C}_3\text{N}_4$ -fluorescein, indicating that photogenerated electrons of fluorescein can be efficiently transferred to the CB of $\text{g-C}_3\text{N}_4$ because there is no overlap between the emission band of fluorescein and the absorption band of $\text{g-C}_3\text{N}_4$. Besides, 3SCN-fluorescein has the lowest carrier recombination, implying that the photoelectrons

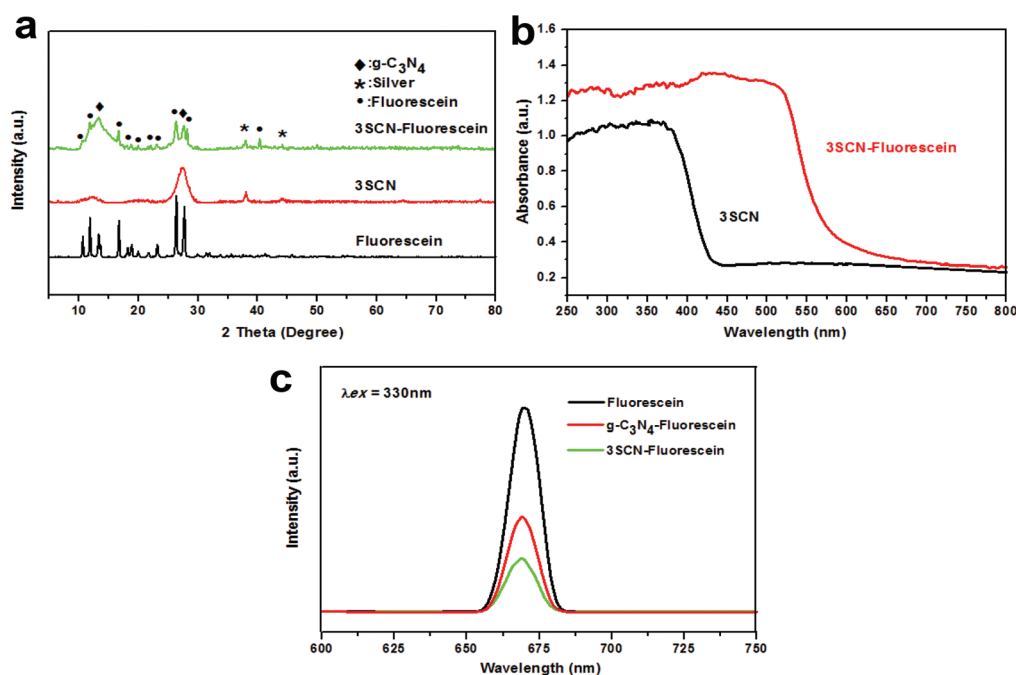


Fig. 11 (a) XRD patterns of fluorescein, 3SCN and 3SCN-fluorescein; (b) UV-vis DRS of 3SCN and 3SCN-fluorescein; (c) PL spectra of fluorescein, $\text{g-C}_3\text{N}_4$ -fluorescein and 3SCN-fluorescein.

are further transferred to Ag particles to improve the quantum efficiency. Consequently, the role of fluorescein and the assumptive mechanism are adequately validated.

Conclusions

In summary, we synthesized a series of Ag/g-C₃N₄ photocatalytic materials with the content of silver in the 1 to 9 wt% range *via* a facile chemical reduction method. Among all the prepared samples, 3% Ag/g-C₃N₄ exhibits the best photocatalytic performance with a hydrogen evolution of 344.51 $\mu\text{mol g}^{-1} \text{h}^{-1}$ under visible light, which is a significant increase compared with that of pure g-C₃N₄ and reported semblable composites. In addition, fluorescein as a photosensitizer contributed to the hydrogen evolution reaching 2014.20 $\mu\text{mol g}^{-1} \text{h}^{-1}$. The photocatalysts possess excellent repeatability. The improved photocatalytic activity mainly depends upon the synergistic effect between the components as well as the appropriate load amount of silver. This paper clearly demonstrates that Ag nanoparticles have feeble catalytic hydrogen production ability and obtaining Ag by chemical reduction was slightly better than by photodeposition. Besides, the sacrificial agent (TEOA) played an important role in hydrogen production. Both the present easy synthetic method of Ag/g-C₃N₄ composites and further study for the photocatalysis process with a dye-photosensitizer provide insights for developing effective photo-catalysts for hydrogen production.

Experimental

Preparation of porous g-C₃N₄

The graphitic C₃N₄ was obtained by directly heating urea.^{9,32,37} In detail, 10.0 g of urea was calcined at 520 °C for 2 h in open air with a heating rate of 5 °C min⁻¹. Then the buff and porous agglomerate was ground into powder in an agate mortar without further treatment.

Synthesis of Ag/g-C₃N₄ nanocomposites

8.0 mL polyethylene glycol (PEG) 600 aqueous solution as a dispersant and a protective agent was added to 8.0 mL of 1.60 mg mL⁻¹ AgNO₃ solution at room temperature to ensure that the mass ratio of AgNO₃ and PEG 600 was 1.5 : 1 and was stirred for 30 min. Subsequently, 9.6 mL NaBH₄ aqueous solution was poured into the above solution rapidly to make the molar ratio of Ag and NaBH₄ 1 : 8, and it was kept stirring for 4 h in an ice water bath. Then, different amounts of g-C₃N₄ were mixed with the above mixture solution by stirring for 20 min and ultrasonication for 1 h. The as-synthesized product was collected by centrifugation, and washed with distilled water three times. Finally, the precipitate was dried at 80 °C overnight. The obtained samples were marked as XSCN, with X representing the quality percentage of Ag with g-C₃N₄ in the reaction and X varied from 1 to 9 in intervals of 2

(1SCN, 3SCN, 5SCN, 7SCN and 9SCN, respectively). The pure g-C₃N₄ served as a contrast.

Pure g-C₃N₄ and Ag/g-C₃N₄ electrodes as working electrodes were prepared as follows: 6 mg of the as-synthesized photocatalyst and 1 cm × 1 cm indium–tin oxide (ITO) glass were submerged in 2 mL absolute ethyl alcohol, and was centrifuged for 1 h at a speed of 4000 rpm. For the samples including fluorescein, an appropriate amount of water was added to the samples dropwise to make a slurry and then the slurry was dripped onto the glass. The electrodes were dried at 120 °C for 1 h. All investigated electrodes have a similar thickness of about 1 μm .

Characterization

The crystal structure of the samples was obtained by using a D8 Advantage X-ray diffraction (XRD, Bruker company, Germany) with Cu K α radiation ($\lambda = 0.15406 \text{ nm}$) in the 2θ range from 5° to 80°. Fourier transform infrared (FTIR) spectra of the materials were recorded on a Bruker Tensor 27 spectrometer using the KBr tableting method. The surface morphologies and the composition of samples were characterized by scanning electron microscopy (SEM, Merlin, Germany) and energy dispersive X-ray spectroscopy (EDS, X-MaxN20, UK), respectively. The crystalline structure and the lattice at HR-TEM modes were analysed on a transmission electron microscope (TEM, JEM-2100HR). X-ray photoelectron spectroscopy (XPS, Axis Ultra DLD, Kratos) was used to analyze the chemical status and composites. Inductively coupled plasma mass spectrometry (ICP-MS, Agilent 7700, Japan) was utilized to confirm the weight percentage of silver in the composite. 5.0 mg of 3SCN was dissolved in 9.0 mL of 65% HNO₃, and then diluted into 388.2 mL of 2% HNO₃. UV-vis diffuse reflectance spectra were obtained on a Hitachi U-3010 spectrophotometer. Photo-luminescence (PL) spectra were recorded by using an F-4500 fluorescence spectrophotometer with an excitation wavelength of 330 nm at room temperature. Raman spectra were obtained by using a Micro Raman spectrometer (LabRAM Aramis, H.J.Y). The Brunauer–Emmett–Teller (BET) specific surface area was recorded by using a surface area and porosity analyzer (ASAP 2020, American) based on nitrogen adsorption and desorption isotherms measured at 77 K. The photocurrents and electrochemical impedance spectra (EIS) were measured by using an electrochemical workstation (CHI660C, China). The as-prepared electrodes served as working electrodes, a platinum flake was used as the counter electrode and Ag/AgCl as the reference electrode. The 0.1 M Na₂SO₄ solution was employed as the electrolyte and a 300 W Xe-lamp served as the light source. The photocurrent intensity of the photocatalysis was measured at 0.0 V with the light on and off. EIS was determined over the frequency range of 100–10⁶ Hz with an ac amplitude of 10 mV at the open circuit voltage.

Photocatalytic activity for hydrogen evolution

Photocatalytic reactions were operated in an outer Pyrex irradiation cell connected to a closed gas circulation system. In

a typical experiment, 0.005 g of the photocatalysts were dispersed in a 70 mL solution containing 10 vol% triethanolamine by using a magnetic stirrer. Before the reaction, the system was thoroughly vacuumed and nitrogen was introduced. The photocatalytic reactions were initiated by using a 300 W Xe-lamp (PLS-SXE300) and the amount of H₂ was analyzed by online GC7900 gas chromatography (TCD detector, 5 Å molecular sieve column).

A series of controlled experiments: the gross amount of the photocatalyst and the mass ratio of Ag are fixed as 0.005 g and 3%, respectively. (1) 5.0 mL of 1.60 mg mL⁻¹ AgNO₃ solution and 1.0 g of PEG 2000 were dispersed in a 70 mL solution containing and excluding 10 vol% triethanolamine, respectively; (2) 0.15 mL of 1.60 mg mL⁻¹ AgNO₃ solution, 1.0 g of PEG 2000 and 4.9 mg of g-C₃N₄ were dispersed in a 70 mL solution containing and excluding 10 vol% triethanolamine, respectively. Calculating H₂ production after an hour light irradiation; (3) 5.0 mg of 3SCN, 1.0 g of PEG 2000 and 5.0 mg of fluorescein were dispersed in a 70 mL solution containing and excluding 10 vol% triethanolamine, respectively. Furthermore, ethylene glycol was substituted for triethanolamine to repeat this experiment.

Acknowledgements

We are extremely grateful to the fund of the Key Laboratory of Fuel Cell Technology of Guangdong Province, the Natural Science Foundation of Guangdong Province (S2013020013091) and the National Natural Science Foundation of China (no. 21571064, 21371060) for financial support.

Notes and references

- Y. T. Gong, M. M. Li, H. R. Li and Y. Wang, *Green Chem.*, 2015, **17**, 715–736.
- Y. F. Chen, W. X. Huang, D. L. He, Y. Situ and H. Huang, *ACS Appl. Mater. Interfaces*, 2014, **6**, 14405–14414.
- J. P. Huo and H. P. Zeng, *J. Mater. Chem. A*, 2015, **3**, 6258–6264.
- Y. J. Wang, Q. S. Wang, X. Y. Zhan, F. M. Wang, M. Safdar and J. He, *Nanoscale*, 2013, **5**, 8326–8339.
- J. Wang, Y.-F. Lim and G. W. Ho, *Nanoscale*, 2014, **6**, 9673–9680.
- Y. L. Tian, B. B. Chang, Z. C. Yang, B. C. Zhou, F. N. Xi and X. P. Dong, *RSC Adv.*, 2014, **4**, 4187–4193.
- J. P. Huo and H. P. Zeng, *J. Mater. Chem. A*, 2015, **3**, 17201–17208.
- A. Fujishima and K. Honda, *Nature*, 1972, **238**, 37.
- E. Z. Liu, L. M. Kang, Y. H. Yang, T. Sun, X. Y. Hu, C. J. Zhu, H. C. Liu, Q. P. Wang, X. H. Li and J. Fan, *Nanotechnology*, 2014, **25**, 165401.
- J. Fu, B. B. Chang, Y. L. Tian, F. N. Xi and X. P. Dong, *J. Mater. Chem. A*, 2013, **1**, 3083–3090.
- H. Y. Liu, K. Y. Zhao, T. T. Wang, J. Y. Deng and H. P. Zeng, *Mater. Sci. Semicond. Process.*, 2015, **40**, 670–675.
- M. J. Muñoz-Batista, A. Kubacka and M. Fernández-García, *Catal. Sci. Technol.*, 2014, **4**, 2006–2015.
- M. Xu, L. Han and S. J. Dong, *ACS Appl. Mater. Interfaces*, 2013, **5**, 12533–12540.
- L. Zhang, D. W. Jing, X. L. She, H. W. Liu, D. J. Yang, Y. Lu, J. Li, Z. F. Zheng and L. J. Guo, *J. Mater. Chem. A*, 2014, **2**, 2071–2078.
- H. Katsumata, T. Sakai, T. Suzuki and S. Kaneco, *Ind. Eng. Chem. Res.*, 2014, **53**, 8018–8025.
- S. Martha, A. Nashim and K. M. Parida, *J. Mater. Chem. A*, 2013, **1**, 7816–7824.
- K. Tian, W.-J. Liu and H. Jiang, *ACS Sustainable Chem. Eng.*, 2015, **3**, 269–276.
- Y. P. Zang, L. P. Li, Y. Zuo, H. F. Lin, G. S. Li and X. F. Guan, *RSC Adv.*, 2013, **3**, 13646–13650.
- S. W. Cao and J. G. Yu, *J. Phys. Chem. Lett.*, 2014, **5**, 2101–2107.
- S. Kumar, T. Surendar, A. Baruah and V. Shanker, *J. Mater. Chem. A*, 2013, **1**, 5333–5340.
- H. F. Shi, G. Q. Chen, C. L. Zhang and Z. G. Zou, *ACS Catal.*, 2014, **4**, 3637–3643.
- J. Wang, P. Guo, M. F. Dou, J. Wang, Y. J. Cheng, P. G. Jonssona and Z. Zhao, *RSC Adv.*, 2014, **4**, 51008–51015.
- H. Xu, Y. X. Song, Y. H. Song, J. X. Zhu, T. T. Zhu, C. B. Liu, D. X. Zhao, Q. Zhang and H. M. Li, *RSC Adv.*, 2014, **4**, 34539–34547.
- B. Hu, F. P. Cai, T. J. Chen, M. S. Fan, C. J. Song, X. Yan and W. D. Shi, *ACS Appl. Mater. Interfaces*, 2015, **7**(33), 18247–18256.
- S. Nayak, L. Mohapatra and K. Parida, *J. Mater. Chem. A*, 2015, **3**(36), 18622–18635.
- S. Pany and K. M. Parida, *Phys. Chem. Chem. Phys.*, 2015, **17**(12), 8070–8077.
- S. Samanta, S. Martha and K. Parida, *ChemCatChem*, 2014, **6**, 1453–1462.
- X. J. Bai, R. L. Zong, C. X. Li, D. Liu, Y. F. Liu and Y. F. Zhu, *Appl. Catal., B*, 2014, **147**, 82–91.
- E. Z. Liu, J. Fan, X. Y. Hu, Y. Hu, H. Li, C. N. Tang, L. Sun and J. Wan, *J. Mater. Sci.*, 2015, **50**, 2298–2305.
- S. Samanta, S. Martha and K. Parida, *ChemCatChem*, 2014, **6**(5), 1453–1462.
- D. B. Ingram, P. Christopher, J. L. Bauer and S. Linic, *ACS Catal.*, 2011, **1**, 1441–1447.
- H. Y. Liu, T. T. Wang and H. P. Zeng, *Part. Part. Syst. Charact.*, 2015, **6**, 1–5.
- L. Ge, C. C. Han, J. Liu and Y. F. Li, *Appl. Catal., A*, 2011, **409–410**, 215–222.
- Y. Y. Bu, Z. Y. Chen and W. B. Li, *Appl. Catal., B*, 2014, **144**, 622–630.
- D. D. Ramos, P. C. S. Bezerra, F. H. Quina, R. F. Dantas, G. A. Casagrande, S. C. Oliveira, M. R. S. Oliveira, L. C. S. Oliveira, V. S. Ferreira, S. L. Oliveira and A. M. Jr, *Environ. Sci. Pollut. Res.*, 2015, **22**, 774–783.

- 36 Y. X. Yang, Y. N. Guo, F. Y. Liu, X. Yuan, Y. H. Guo, S. Q. Zhang, W. Guo and M. S. Huo, *Appl. Catal., B*, 2013, **142–143**, 828–837.
- 37 W. Zhang and R. Xu, *Int. J. Hydrogen Energy*, 2012, **37**, 17899–17909.
- 38 J. Zhang and X. H. Liu, *Phys. Chem. Chem. Phys.*, 2014, **16**, 8655–8660.
- 39 Y.-P. Yuan, L.-S. Yin, S.-W. Cao, G.-S. Xu, C.-H. Li and C. Xue, *Appl. Catal., B*, 2015, **168**, 572–576.
- 40 T. T. Jia, M. J. Li, L. Ye, S. Wiseman, G. L. Liu, J. Qu, K. Nakagawa and E. Tsang, *Chem. Commun.*, 2015, **51**(70), 13496–13499.
- 41 L. J. Yu, X. H. Zhang, C. S. Zhuang, L. Lin, R. J. Li and T. Y. Peng, *Phys. Chem. Chem. Phys.*, 2014, **16**, 4106–4114.
- 42 P. W. Zhou, J. Y. Liu, S. Q. Yang, J. S. Chen, K. L. Han and G. Z. He, *Phys. Chem. Chem. Phys.*, 2012, **14**, 15191–15198.
- 43 M.-C. Rosu, R.-C. Suciuc, M. D. Lazar and I. Bratu, *Mater. Sci. Eng., B*, 2013, **178**, 383–390.
- 44 H. Y. Zhang, S. Li, R. Lu and A. C. Yu, *ACS Appl. Mater. Interfaces*, 2015, **7**(39), 21868–21874.
- 45 H. Q. Qian, H. Y. Mao, F. Song, S. Q. Shi, H. J. Zhang, H. Y. Li, P. M. He and S. N. Bao, *Appl. Surf. Sci.*, 2010, **256**, 2686–2690.
- 46 B. Chai, T. Y. Peng, J. Mao, K. Lia and L. Zan, *Phys. Chem. Chem. Phys.*, 2012, **14**, 16745–16752.
- 47 K. Cao, Z. Y. Jiang, X. S. Zhang, Y. M. Zhang, J. Zhao, R. S. Xing, S. Yang, C. Y. Gao and F. S. Pan, *J. Membr. Sci.*, 2015, **490**, 72–83.
- 48 T. Dittrich, S. Fiechter and A. Thomas, *Appl. Phys. Lett.*, 2011, **99**(8), 084105.
- 49 S. Q. Huang, Y. G. Xu, M. Xie, H. Xu, M. Q. He, J. X. Xia, L. Y. Huang and H. M. Li, *Colloids Surf., A*, 2015, **478**, 71–80.
- 50 J. Q. Tian, Q. Liu, A. M. Asiri, X. P. Sun and Y. Q. He, *Sens. Actuators, B*, 2015, **216**, 453–460.
- 51 T. T. Zhu, Y. H. Song, H. Y. Ji, Y. G. Xu, Y. X. Song, J. X. Xia, S. Yin, Y. P. Li, H. Xu, Q. Zhang and H. M. Li, *Chem. Eng. J.*, 2015, **217**, 96–105.
- 52 Z. H. Chen, P. Sun, B. Fan, Q. Liu, Z. G. Zhang and X. M. Fang, *Appl. Catal., B*, 2015, **170–171**, 10–16.
- 53 B. C. Zhu, P. F. Xia, W. K. Ho and J. G. Yu, *Appl. Surf. Sci.*, 2015, **344**, 188–195.
- 54 Z. F. Jiang, D. Liu, D. L. Jiang, W. Wei, K. Qian, M. Chen and J. M. Xie, *Dalton Trans.*, 2014, **43**, 13792–13802.
- 55 J. P. Huo, L. T. Fang, Y. L. Lei, G. C. Zeng and H. P. Zeng, *J. Mater. Chem. A*, 2014, **2**, 11040–11044.
- 56 J. Z. Jiang, L. H. Zhu, J. Zou, L. Ou-Yang, A. M. Zheng and H. Q. Tang, *Carbon*, 2015, **87**, 193–205.
- 57 J. Z. Jiang, L. Ou-Yang, L. H. Zhu, J. Zou and H. Q. Tang, *Sci. Rep.*, 2014, **3942**, 1–9.
- 58 F. He, G. Chen, Y. G. Yu, S. Hao, Y. S. Zhou and Y. Zheng, *ACS Appl. Mater. Interfaces*, 2014, **6**, 7171–7179.
- 59 X. H. Zhang, T. Y. Peng, L. J. Yu, R. J. Li, Q. Q. Li and Z. Li, *ACS Catal.*, 2015, **5**, 504–510.
- 60 Y. P. Yuan, W. T. Xu, L. S. Yin, S. W. Cao, Y. S. Liao, Y. Q. Tng and C. Xue, *Int. J. Hydrogen Energy*, 2013, **38**, 13159–13163.
- 61 Y. N. Feng, C. Chen, Z. G. Liu, B. J. Fei, P. Lin, Q. P. Li, S. G. Sun and S. W. Du, *J. Mater. Chem. A*, 2015, **3**(13), 7163–7169.